## PAPER

Check for updates

# Study on the synthesis of nano-hydroxyapatite assisted by sodium dodecyl sulfate significantly enhances the adsorption performance of rhodamine B

Ya-Ni Zhang, Qiu-Yan Yang, Peng Wang, Jia-Hui Li, Shu-Yao Zhang, En-Peng Deng, Xue-Min Wang, Jipeng Meng and Yu-Xin Miao [ID] *

In this study, we synthesized sodium dodecyl sulfate modified hydroxyapatite (SDS-HAP) to enhance the removal efficiency of rhodamine B (RhB) dye. The SDS-HAP prepared using the sol−gel method exhibited a significantly higher adsorption capacity compared to pristine HAP. Various characterization techniques, including X-ray diffraction (XRD), $N_2$ adsorption−desorption isotherms, Fourier-transform infrared spectroscopy (FT-IR), and scanning electron microscopy (SEM), were utilized to systematically investigate the morphological and structural changes. Batch experiments were conducted to evaluate the influence of RhB concentration, pH value, temperature, dosage, and contact time on the adsorption performance. Results indicated that the addition of SDS increased the specific surface area from 72.8 to 136.8 $m^2$ $g^{-1}$. The equilibrium adsorption capacity of SDS-HAP for RhB was approximately 3.3 times greater than that of pure HAP. Kinetic studies revealed rapid equilibrium following the pseudo-second-order model ($R^2 = 0.9999$). The Freundlich isotherm model best described the experimental data, with a maximum adsorption capacity of 44.1 mg $g^{-1}$. Thermodynamic analysis confirmed that the adsorption process was spontaneous, endothermic, and driven by hydrogen bonding and electrostatic interactions between the dye molecules, $PO_4^{3-}$, $Ca^{2+}$ and $OH^-$.

## 1. Introduction

The rapid advancement of industrial processes has led to the extensive discharge of inadequately treated wastewater, severely contaminating global water systems. Aquatic pollutants appear in diverse forms, including synthetic dyes, metallic contaminants, agricultural chemicals, and pharmaceutical derivatives. Notably, the textile printing and dyeing industry is regarded as one of the most polluting sectors.[1] These chromatic pollutants exhibit significant environmental persistence and bioaccumulation potential, positioning them as primary aquatic contaminants.[2] Consequently, there is an urgent need to develop an environmentally friendly and cost-effective approach for wastewater treatment.[3]

Contemporary wastewater treatment methodologies incorporate a variety of advanced technological approaches, including membrane filtration, contaminant immobilization, coagulation–flocculation processes, redox precipitation, photochemical decomposition, and electro-assisted purification.[4] Among these, the adsorption method is regarded as an optimal approach for

treating toxic pollutants in wastewater due to its simplicity, high efficiency, low cost, and minimal risk of secondary pollution[5] This technique exhibits broad-spectrum efficacy against a wide array of pollutants, achieving significant purification levels while enabling material regeneration *via* controlled release mechanisms—a critical feature that aligns with circular economy principles. In recent years, researchers have developed a diverse range of adsorbents, including clay minerals, zeolites, bio-based materials, nanomaterials, and ion exchange resins.[6] While conventional porous carbon materials demonstrate significant contaminant uptake capacity, their practical application is constrained by low regeneration efficiency and environmental sensitivity. Biogenic substrates, although offering ecological advantages, often exhibit inconsistent performance at the industrial scale. Advanced nanomaterials, despite their technological superiority, face cost barriers and potential ecotoxicological risks. Each material system presents distinct benefit–cost profiles, necessitating careful selection based on operational requirements and sustainability considerations. Future research should focus on developing composite materials and optimizing adsorption conditions to enhance both efficiency and environmental compatibility.

Hydroxyapatite (HAP), a calcium phosphate mineral, has emerged as a versatile medium for mitigating aquatic

*Institute of Catalysis for Energy and Environment, College of Chemistry and Chemical Engineering, Shenyang Normal University, Shenyang, 110034, P. R. China. E-mail: yuxinmiao@synu.edu.cn; Tel: +86-24-86578847*

contaminants, demonstrating particular efficacy against metallic species, synthetic dyes, and emerging micropollutants.[7] HAP exhibits strong interactions with dye molecules owing to its mechanical stability, modifiable surface groups, low water solubility, and high adsorption capacity.[8] The mineral's crystalline architecture facilitates electrostatic interactions between its dual-charged ionic components ($Ca^{2+}$ and $PO_4^{3-}$) and target contaminants, thereby enabling efficient pollutant capture.[9] These characteristics, coupled with low toxicity and economic feasibility, have driven the widespread adoption of HAP in environmental engineering, biomedical applications, and materials science.[10] The sol–gel fabrication technique has become predominant in HAP research, yielding monodisperse nanoparticles that exhibit optimal optical properties, colloidal stability, and biocompatibilit.[11] However, pure HAP tends to aggregate in aqueous solutions, thereby reducing its dispersion and adsorption capacity. Furthermore, in the synthesis of nanomaterial HAP, it is easy to be chemically modified by various functional groups.[12] Existing studies have shown that modification HAP by synthesizing surfactants can effectively alleviate this problem, thereby improving the overall performance of the adsorbent.[13] Sodium dodecyl sulfate (SDS), an economical anionic surfactant, exhibits remarkable dispersion capabilities and interfacial activity.[14] Its unique ability to control dimensions at the nanoscale and its broad industrial applicability, especially in cleaning formulations, make it particularly suitable for material modification.[15] By enhancing the specific surface area and dispersibility of HAP, SDS significantly improves its adsorption performance.

In this study, we conducted a comprehensive investigation into the adsorption properties of SDS-HAP, which was synthesized *via* the sol–gel method, toward RhB for the first time. Additionally, we meticulously analyzed the adsorption isotherms, kinetics and mechanisms. The SDS-HAP system exhibits remarkable cost-effectiveness and environmental safety, making it a highly promising platform for aquatic environment remediation. Future research will concentrate on further exploring the application of RhB adsorption to enhance both adsorption efficiency and regeneration performance. These efforts hold great significance for both environmental protection and public health.

## 2. Experimental

### 2.1. Adsorbent preparation

0.01 mol of $Ca(NO_3)_2 \cdot 4H_2O$ was dissolved in 100 mL of deionized water. Varying amounts of SDS (0, 0.1, 0.5, 1.0, 1.5, and 2.0 g) were subsequently added to the solution in a water bath maintained at 50 °C. Next, 0.006 mol of $H_3PO_4$ was introduced into the mixture, and the pH was adjusted to 9.5 using ammonia solution. After ensuring complete reaction, the mixture was cooled to room temperature and allowed to stand for 24 hours. The resulting precipitate was then centrifuged, washed, and subjected to freeze-drying. This procedure yielded a series of white fluffy powder products doped with different amounts of SDS, designated as fresh HA, HA0.1, HA0.5, HA1.0, HA1.5 and HA2.0. All chemicals used were of analytical grade

and were utilized without further purification. Deionized water served as the solvent for preparing all dye solutions throughout the adsorption experiments.

### 2.2. Catalyst characterization

The X-ray diffraction (XRD) patterns were recorded using a Rigaku Ultima IV diffractometer with Cu Kα radiation at 40 kV and 30 mA, and the scanning was performed at a rate of $5° \text{ min}^{-1}$ within the $2\theta$ range of 20–60°. The Micromeritics ASAP 2460 fully automatic specific surface area analyzer was used to analyze the specific surface area, porosity and pore size distribution of the experimental samples. A nitrogen adsorption–desorption isotherm test was carried out at liquid nitrogen temperature (77 K). An infrared spectrometer (Bruker TENSOR II) produced by Bruker Corporation in Germany was used to identify the functional groups on the surface of HAP within the wavenumber range of 300–4000 $\text{cm}^{-1}$ *via* an Attenuated Total Reflection (ATR) accessory. The morphology of HAP was observed using scanning electron microscopy (SEM) on a Hitachi S-4800. Ultraviolet/Visible/Near-Infrared (UV-Vis-NIR) absorption spectra recorded with a Hitachi UH5300 Spectrophotometer, was used to measure the absorbance of the analytes from visible to ultraviolet light (300–800 nm) and conduct quantitative analysis.

### 2.3. Batch adsorption study

As shown in Fig. 1, a 10 mg per L RhB solution was accurately prepared and then diluted to concentrations of 2, 4, 6, 8, and 10 mg $\text{L}^{-1}$. The absorbance values were determined at a wavelength of 554 nm using ultraviolet-visible (UV-Vis) spectroscopy, and a corresponding standard calibration curve was established. The linear regression equation obtained was $y = 0.194x - 0.0104$, with a coefficient of determination ($R^2$) of 0.9997. Eqn (1)–(3) were subsequently applied to calculate the equilibrium adsorption capacity and the adsorption rate. The effects of various parameters, including adsorbent dosage, contact time, reaction temperature, initial RhB concentration, and pH, on the adsorption efficiency of RhB were systematically investigated within an
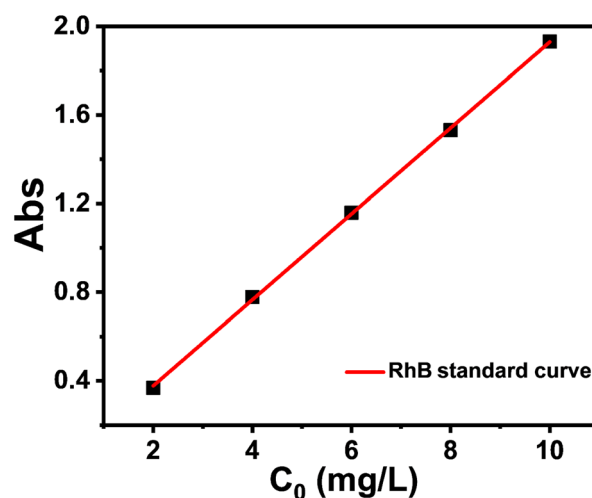


**Fig. 1** Standard absorbance curve of RhB under different dilution concentrations at 554 nm.

initial RhB concentration range of 10 to 50 mg L$^{-1}$. Adsorption kinetic and isotherm experiments were carried out under controlled laboratory conditions at a constant temperature of 25 °C and a fixed pH. Preliminary experimental results showed that directly adding SDS to the RhB solution did not substantially enhance the adsorption efficiency. When 50 mg of HA was used to treat RhB solution ($C_0 = 10$ mg L$^{-1}$, $V = 50$ mL), the removal

rate was only 27.9%, indicating limited adsorption capacity. In contrast, the SDS-modified sample HA0.5 (50 mg) achieved a removal rate of up to 99.5%, demonstrating a significant improvement in adsorption performance. However, further increasing the SDS dosage to 1 g (HA1.0 sample) resulted in a slight decrease in removal efficiency to 97.8% under the same experimental conditions. Therefore, the HA0.5 sample was selected for subsequent investigations, as illustrated in Fig. 2.
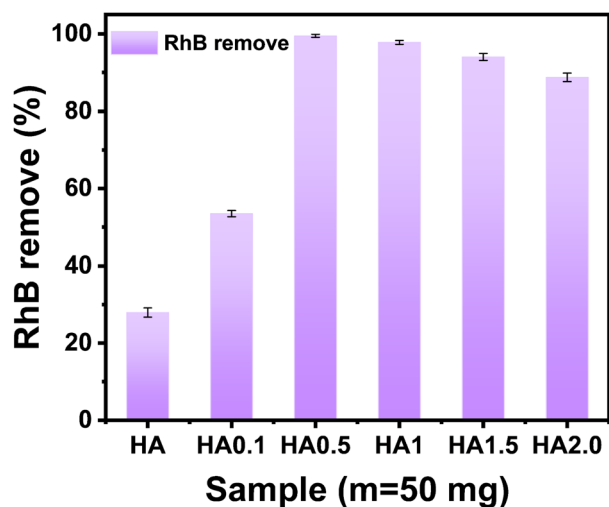
$$q_e = (C_0 - C_e) \times V/m \qquad (1)$$

$$q_t = (C_0 - C_t) \times V/m \qquad (2)$$

$$R\% = (C_0 - C_e)/C_0 \times 100\% \qquad (3)$$

where $q_e$ (mg g$^{-1}$) is the equilibrium adsorption capacity, $V$ (L) is the volume of dye solution, $m$ (g) is the adsorbent mass, $C_t$ (mg L$^{-1}$) is the RhB concentration at time $t$, $R$ (%) is the adsorption rate, $C_0$ (mg L$^{-1}$) is the initial dye concentration, and $C_e$ (mg L$^{-1}$) is the equilibrium dye concentration.

## 3. Results and discussion

### 3.1. Characterization of adsorbent

The crystal phase and corresponding crystallite sizes were characterized using XRD patterns for both HAP and SDS-HAP samples, as illustrated in Fig. 3(a). The characteristic
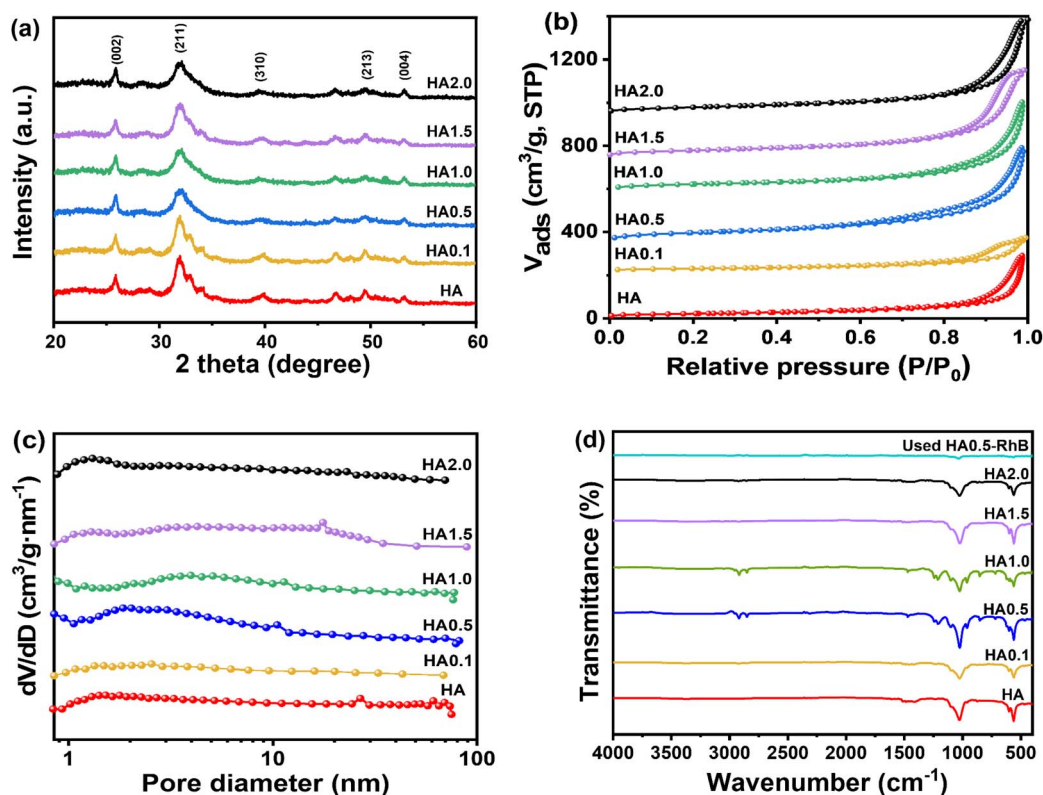


**Fig. 2** The removal rates of RhB ($C_0 = 10$ mg L$^{-1}$, $V = 50$ mL) by different samples.



**Fig. 3** (a) XRD patterns of HA, HA0.1, HA0.5, HA1.0, HA1.5 and HA2.0, (b) the N$_2$ adsorption–desorption curves of HA0.1, HA0.5, HA1.0, HA1.5 and HA2.0 are shifted upward by 200, 360, 600, 750, 950 cm$^3$ per g STP, (c) pore size distribution of adsorbent, (d) FT-IR spectra of HA, HA0.1, HA0.5, HA1.0, HA1.5, HA2.0 and used HA0.5-RhB.

diffraction peaks align with those reported in the JCPDS standard card (No. 09-0432), confirming that the synthesized samples exhibit a hexagonal structure typical of HAP. Specifically, the crystal planes at $2\theta$ angles of 25.9°, 31.8°, 32.2°, 32.9°, 34.0°, 39.8°, 49.5°, and 53.1° correspond to the (002), (211), (112), (300), (202), (310), (213) and (004) planes of HAP, respectively. Notably, after incorporating a certain amount of SDS, the intensity of the characteristic diffraction peaks for the (002), (213) and (004) planes increased, indicating enhanced crystallinity of HAP.

Fig. 3(b) shows the $N_2$ adsorption and desorption isotherm of the sample. The isotherms exhibit typical type IV behavior with H3 hysteresis loops, indicating the presence of mesoporous structures in the prepared carriers. Table 1 summarizes the specific surface area (SSA) and pore volume information of the material. The SSA of the HAP sample prepared by us was 72.8 m$^2$ g$^{-1}$. The addition of SDS increased the SSA, however, this increase did not correlate linearly with the SDS concentration, with the HA0.5 sample exhibiting the highest SSA. As shown in Fig. 3(c), there was no significant difference in pore size distribution among the samples, which ranged from 9 to 13 nm. This uniformity in pore size may be attributed to the SDS concentration in the solution.

The Fourier transform infrared (FTIR) spectra were recorded between 4000 and 400 cm$^{-1}$ to identify the hydroxyl and phosphate groups on the surface of HAP.[16] As shown in Fig. 3(d), characteristic absorption bands at wavenumbers 562 cm$^{-1}$, 600 cm$^{-1}$, and 586 cm$^{-1}$ were attributed to the bending and stretching vibrations of the O–P–O bonds in the phosphate ($PO_4^{3-}$) group on the surface of HAP.[17–19] The subsequent absorption band at 871 cm$^{-1}$ was assigned to the hydrogen phosphate radical ($HPO_4^{2-}$).[20] Additionally, the triplet of absorption bands peaking at 963 cm$^{-1}$ and 1026 cm$^{-1}$ were ascribed to distinct vibrational modes of the P–O bonds within the $PO_4^{3-}$ groups.[21] The peak observed at approximately 1108 cm$^{-1}$ could correspond to the S=O vibration.[22] Acetate ions exhibit symmetric C–O stretching modes at 1414 cm$^{-1}$, indicating that $CO_2$ participates in the reaction and replaces $PO_4$.[3–23] The broad bands at 1673 cm$^{-1}$ and 3372 cm$^{-1}$ can be attributed to the H–O–H bending vibration mode in the water lattice. In the range of 2800–3000 cm$^{-1}$, a decrease in peak intensity suggests that some SDS may have been washed off.

The morphology and structure of HAP prepared by the sol–gel method and some samples after adding SDS were characterized by scanning electron microscopy (SEM) in Fig. 4. HAP exhibits a lamellar structure in the shape of thin flakes, with a size of approximately 10 to 100 nm. The single lattice spacing of 0.82 nm was calculated by transmission electron microscopy, which corresponded to HAP (111) crystal plane by comparing with standard card. After adding SDS, HAP gradually transforms into a more irregular flocculent morphology, stacking in a disorderly manner and forming a well-dispersed lamellar material with numerous voids. As the amount of SDS added increases, the area of the thin flakes further expands.

## 3.2. Effect of adsorbent dosage

Different masses of HA0.5 adsorbent were added to 50 mL of 20 mg per L RhB solution and shaken at 25 °C in a constant temperature shaker for 1 hour. Afterward, the supernatant was filtered through a 0.22 μm microfilter, and absorbance values were measured using a UV spectrophotometer. The adsorption capacity and removal rate were then calculated according to the formula to investigate the influence of adsorbent dosage. As shown in Fig. 5, the removal of RhB initially increased rapidly with increasing adsorbent amount but subsequently leveled off. Conversely, the adsorption capacity exhibited an opposite trend. At an adsorbent dosage of 0.05 g, the removal rate of RhB reached 97.2%, with an equilibrium adsorption capacity of 15.1 mg g$^{-1}$. The decrease in adsorption capacity may be attributed to the limited number of effective adsorption sites, leading to reduced effectiveness per unit mass of adsorbent during the process.[24] Beyond this point, further increases in adsorbent amount did not significantly enhance the removal rate, as the adsorption capacity gradually approached saturation equilibrium. To achieve near-complete adsorption of RhB, we selected 0.05 g of adsorbent as the optimal condition for subsequent experiments.

## 3.3. Effect of concentration and adsorption time on RhB adsorption

The influence of different initial concentrations and contact time on RhB adsorption is illustrated in Fig. 6. This experiment was conducted over a concentration range from 10 to 50 mg L$^{-1}$, with identical experimental conditions and procedures to investigate the effect of equilibrium time. Specifically, 0.05 g of HA0.5 adsorbent was added to 50 mL of RhB solution at various initial concentrations and subjected to constant temperature shaking at 25 °C. Samples were collected and filtered at intervals of 5, 10, 15, 20, 40, 60, 80, 100, and 120 minutes, and absorbance values were measured using a UV spectrophotometer. The adsorption capacity and removal rate were then calculated.

The adsorption of RhB is significantly influenced by the initial concentration. As the initial concentration increases, the adsorption amount initially rises rapidly before gradually approaching equilibrium. The results indicate that the adsorption capacity increases with the enhanced collision frequency between the adsorbent and RhB molecules, providing
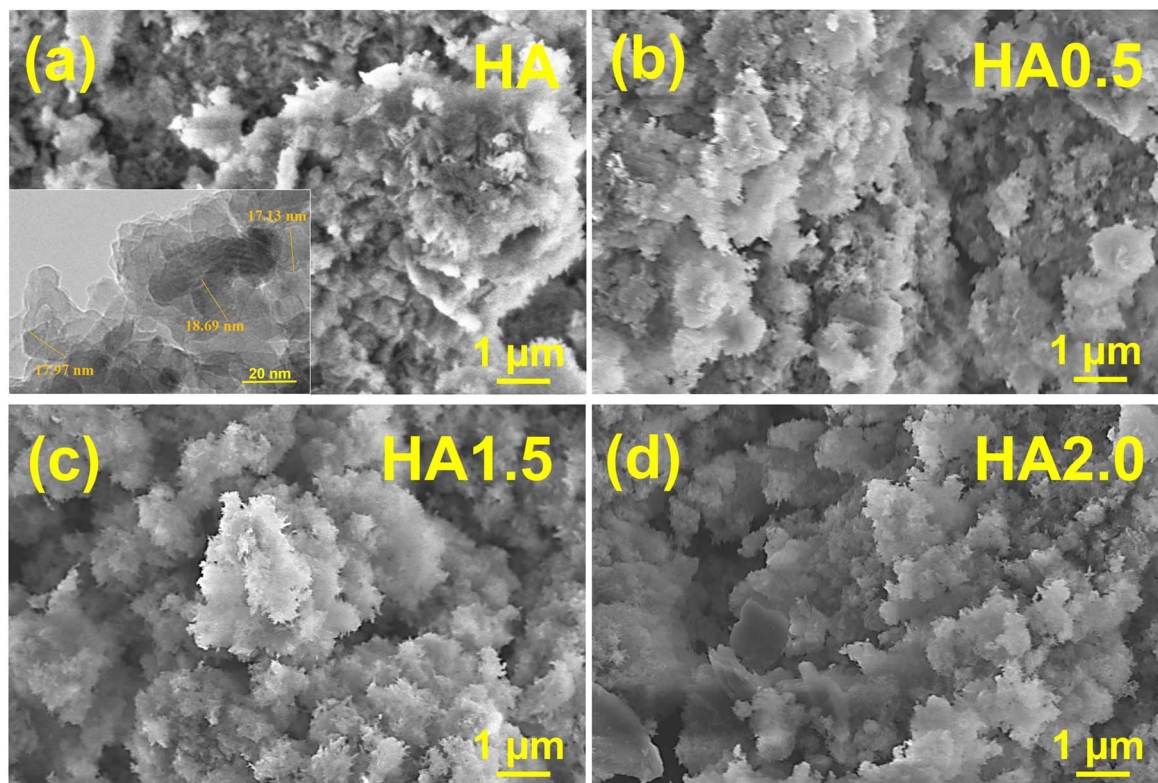
**Table 1** Physicochemical properties of different samples

| Sample | $S_{BET}^a$ (m$^2$ g$^{-1}$) | $D_v^b$ (cm$^3$ g$^{-1}$) | $D_p^b$ (nm) |
|---|---|---|---|
| HA | 72.8 | 0.5 | 12.4 |
| HA0.1 | 44.3 | 0.2 | 10.8 |
| HA0.5 | 136.8 | 0.7 | 9.7 |
| HA1.0 | 96.6 | 0.5 | 10.2 |
| HA1.5 | 129.8 | 0.6 | 9.7 |
| HA2.0 | 119.0 | 0.7 | 11.4 |

$^a$ The $S_{BET}$ of sample were determined by the Brunauer–Emmett–Teller (BET) method. $^b$ $D_v/V_p$ was the average pore diameter/average pore volume which was calculated by the BJH method.

**Fig. 4** SEM images of HA (a), HA0.5 (b), HA1.5 (c), HA2.0 (d) and TEM image of HA embedded in (a).
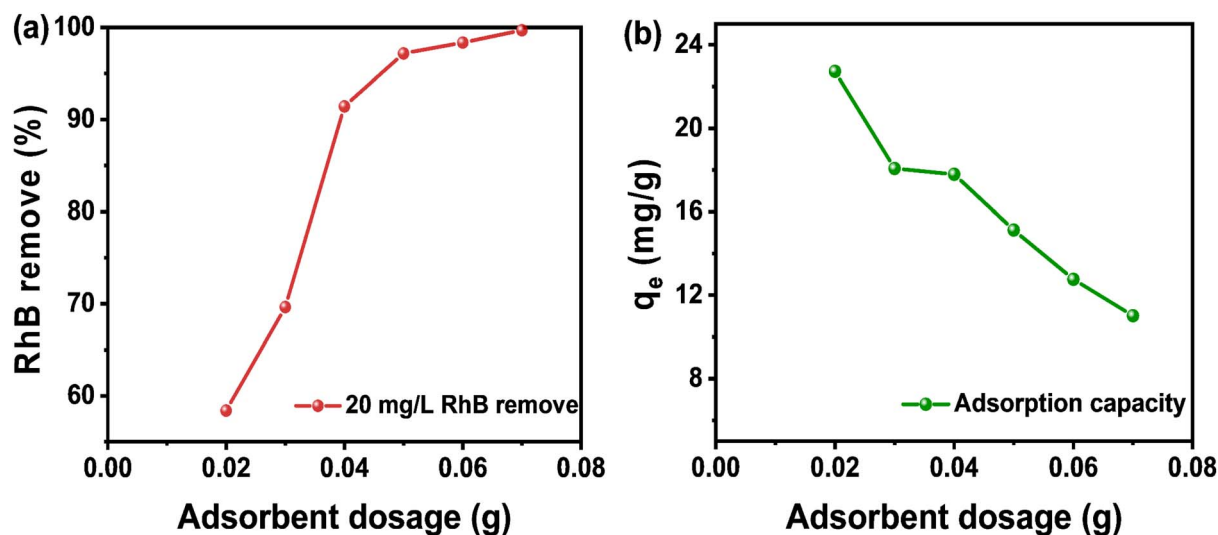


**Fig. 5** Effect of adsorbent dosage on RhB remove (a) and adsorption (b).

numerous adsorption sites for RhB. Over time, as some adsorption sites on the surface of the adsorbent become occupied, the adsorption process tends toward equilibrium and eventually reaches saturation. At an initial solution concentration of 50 mg L$^{-1}$, the maximum adsorption capacity reached 44.1 mg g$^{-1}$.

In the first 20 minutes of the reaction, the adsorption capacity increased rapidly due to the availability of numerous

unoccupied adsorption sites on the adsorbent surface, allowing for the rapid uptake of RhB molecules. As time progressed, the system approached equilibrium after 1 hour of reaction. Experimental results showed that the adsorption remained stable after 12 hours. This stability can be attributed to two factors: (1) the surface of the adsorbent being extensively occupied by RhB molecules, leading to electrostatic repulsion, and (2) the reduction in available active sites on the adsorbent
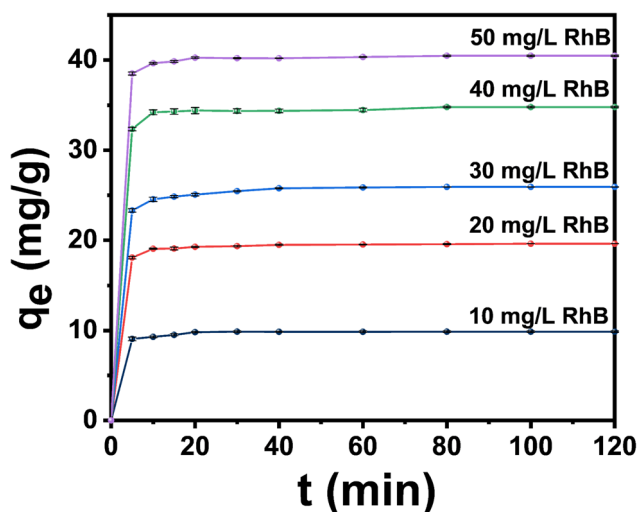
Paper

Fig. 6 Effect of adsorption time and concentration on adsorption of RhB.

surface, which limits further adsorption and gradually leads to equilibrium.

### 3.4. Influence of initial pH value and temperature on RhB adsorption

The pH value condition plays a crucial role in the adsorption of RhB by the adsorbent, as changes in the pH value can influence the surface chemistry of both the dye and the adsorbent, as well as the degree of ionization of RhB molecules. Adsorption experiments were conducted by adding 0.05 g of adsorbent to 50 mL of 20 mg per L RhB solution at various pH value levels. As shown in Fig. 7(a), the adsorption rate and capacity exhibited an initial increase followed by a decrease with increasing solution pH. Within the pH value range of 5–9, the removal rate and adsorption capacity changed gradually. Under strongly acidic conditions, the removal rate decreased due to excessive $H^+$ ions

in the solution reacting with $^{\cdot}OH$ groups, leading to the consumption of active species. Additionally, electrostatic repulsion and competitive adsorption between RhB cations and $H^+$ ions limited the adsorption of RhB and other cationic dyes.[25] Under strongly alkaline conditions, the adsorption capacity slightly decreased, possibly due to structural damage and changes in some adsorption sites on the surface.

At pH value of 7, the adsorption performance was optimal, achieving a removal rate of 97.2% and a maximum adsorption capacity of 19.6 mg g$^{-1}$. This is attributed to the dissociation of functional groups on the surface, which enhances the attraction between the dye molecules and the adsorbent, thereby improving the adsorption capacity.[26] Similar trends have been reported by Khan et al.,[27] who noted that within the entire pH range of 2–13, the adsorption rate for RhB remained above 92%, demonstrating excellent adsorption performance.

Adsorption experiments were conducted by adding 0.05 g of adsorbent to 50 mL of 20 mg per L RhB solution at various temperatures. As shown in Fig. 7(b), the adsorption rate and capacity of the adsorbent material for RhB increased with rising temperature. The increase in temperature enhances the adsorption affinity of the sample for RhB, which can be attributed to the increased mobility of active sites on both the dye molecules and the adsorbent. This phenomenon may be due to faster diffusion of dye molecules at higher temperatures, facilitating their entry into the pores of the adsorbent.[28] When compared with several other HAP composites in Table 2, the SDS-modified HAP adsorbent exhibits a remarkable adsorption capacity. This characteristic suggests that it has significant potential for effectively adsorbing high-concentration dyes. Therefore, we then analyzed the isothermal adsorption model, kinetic and thermodynamic data in order to better understand the adsorption mechanism.

### 3.5. Adsorption isotherm study

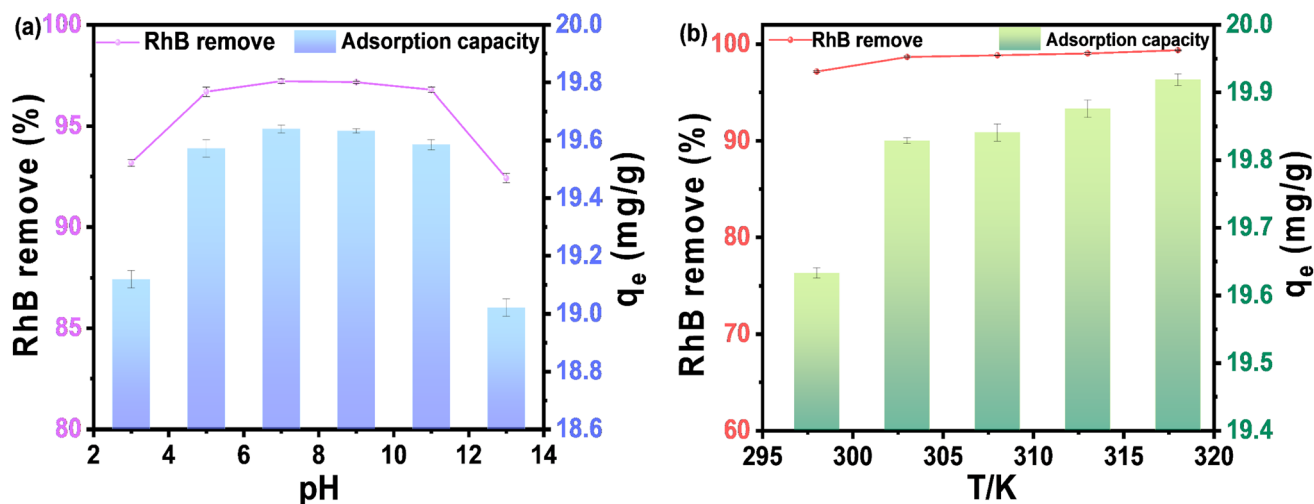The adsorption isotherm model, serving as a representation of equilibrium data, plays a pivotal role in the in-depth



Fig. 7 (a) Influence of initial pH value on RhB adsorption and (b) effect of temperature on adsorption of RhB.

**Table 2** Physicochemical properties of different samples

| Sample | SSA ($m^2 \ g^{-1}$) | $C_0$ (mg $L^{-1}$) | pH | $q_m$ | References |
|---|---|---|---|---|---|
| GO | 833 | 25 | 3 | 13.5 | 29 |
| Red-clay | 22.4 | 40 | 5 | 18.8 | 30 |
| Hide substance-chitosan-HAP | $5.5 \times 10^{-5}$ | 50 | 12 | 3.8 | 31 |
| HAP-Fe$_3$O$_4$ | 75.2 | 40 | — | 12.4 | 32 |
| HAP-biochar | 127.1 | 50 | 8 | 21.1 | 33 |
| HA0.5 | 136.8 | 50 | 7 | 44.1 | This work |

investigation of the adsorption process mechanism. This model elucidates the relationship between the adsorbent and adsorbate, characterizing the interaction on the adsorbent surface and assessing the adsorption capacity. In this study, four distinct isotherm models—Freundlich, Langmuir, Temkin, and Dubinin–Radushkevich (D–R)—were utilized to describe the adsorption behavior of RhB on SDS-HAP. The experimental results reveal that these models exhibit varying degrees of correlation with the experimental data. Table 3 provides a comprehensive summary of all parameters associated with the four isotherms.

In Fig. 8(a), the Freundlich isotherm model is employed to describe multilayer adsorption involving interactions between adsorbed molecules.[34] A $1/n$ value within the range of 0.1–1 suggests favorable conditions for the adsorption process.[35] The Freundlich model demonstrates a good fit ($R^2 = 0.9712$), with the result approaching unity.

**Table 3** The isothermal adsorption model parameters and kinetic parameters of HA0.5 adsorbing RhB

| Isotherm model | Equations | Parameters |
|---|---|---|
| Langmuir | $C_e/q_e = C_e/q_m + 1/(K_L q_m)$<br>$R_L = 1/(1 + K_L C_0)$ | $q_m = 45.96$<br>$K_L = 1.20$<br>$R^2 = 0.9518$ |
| Freundlich | $\lg q_e = \lg K_F + 1/n \lg C_e$ | $n = 2.71$<br>$K_F = 21.86$<br>$R^2 = 0.9712$ |
| Temkin | $q_e = A \ln K_T + A \ln C_e$<br>$A = RT/b$ | $A = 8.31$<br>$K_T = 20.29$<br>$R^2 = 0.9413$ |
| D–R | $\ln q_e = \ln q_m - K\varepsilon^2$<br>$\varepsilon = RT \times \ln(1 + 1/C_e)$<br>$E = 1/(2K^{0.5})$ | $K = 5.04 \times 10^{-8}$<br>$E = 3.15$<br>$R^2 = 0.8735$ |

| Kinetic model | Equations | Kinetic constant |
|---|---|---|
| Pseudo-first-order | $\ln(q_e - q_t) = \ln q_e - k_1 t$ | $q_{e,exp} = 3.05$<br>$k_1 = 0.14$<br>$R^2 = 0.8699$ |
| Pseudo-second-order | $t/q_t = (1/k_2 q_e^2) + t/q_e$ | $q_{e,exp} = 9.93$<br>$k_2 = 0.26$<br>$R^2 = 0.9999$ |
| Elovich model | $q_t = \alpha + \beta \ln t$ | $\alpha = 0.36$<br>$\beta = 8.52$<br>$R^2 = 0.8658$ |
| Intraparticle diffusion | $q_t = k_i t^{0.5} + C$ | $k_i = 0.15$<br>$C = 8.88$<br>$R^2 = 0.7066$ |

The feasibility of representing Langmuir isotherm behavior is assessed using the dimensionless separation factor $R_L$.[36] $R_L$ values (see Table 3) characterize the isotherm shape: specifically, $0 < R_L < 1$ indicates favorable adsorption, $R_L = 0$ signifies irreversible adsorption, $R_L = 1$ denotes linear adsorption, and $R_L > 1$ implies unfavorable adsorption.[37] In this study, $R_L = 0.04$ ($0 < R_L < 1$), confirming that the surface adsorption process is favorable. Furthermore, monolayer adsorption, as evidenced by the Langmuir model ($R^2 = 0.9518$), plays a significant role in dye molecule adsorption. The maximum adsorption capacity was determined to be 45.96 mg $g^{-1}$.

The Dubinin–Radushkevich (D–R) equation is grounded in the micropore-filling theory, wherein the pore volume is progressively filled based on the adsorption potential. The $E$ value serves as a critical parameter for identifying the type of adsorption mechanism. Specifically, when $E < 8$ kJ $mol^{-1}$, the adsorption process is predominantly governed by physical forces. When $8 < E < 16$ kJ $mol^{-1}$, the adsorption mechanism shifts to being controlled by chemical ion exchange. When $E > 16$ kJ $mol^{-1}$, particle diffusion becomes the dominant factor influencing adsorption.[38] In this study, the adsorption energy value obtained from the D–R isotherm was $E = 3.15$ kJ $mol^{-1}$. This relatively low value provides strong evidence that the adsorption of RhB onto HA0.5 is primarily driven by physical interactions.

In general, the Temkin isotherm model assumes that adsorption enthalpies decrease linearly with an increase in coverage and that binding energy is uniformly distributed up to a certain maximum binding energy.[39] However, the low fitted correlation coefficient for this model suggests that it is not appropriate for describing the adsorption behavior observed in this experiment. In contrast, the Freundlich model, which exhibits a significantly higher correlation coefficient, provides a better description of the RhB adsorption behavior. The experimental adsorption process on the surface can be attributed to a multi-layer adsorption mechanism occurring on a heterogeneous surface.

### 3.6. Adsorption kinetics study

The potential mechanisms of dye adsorption and the possible rate-controlling steps can be investigated by establishing kinetic models.[40] This study presents the calculated parameters and validation outcomes for four kinetic models as shown in Table 3. The results of linear fitting are illustrated in Fig. 9.

Where, $q_e$ and $q_t$ are the amounts of RhB sorbed (mg $g^{-1}$) at equilibrium and at any time, $t$ respectively, and $k_1$ is the pseudo-
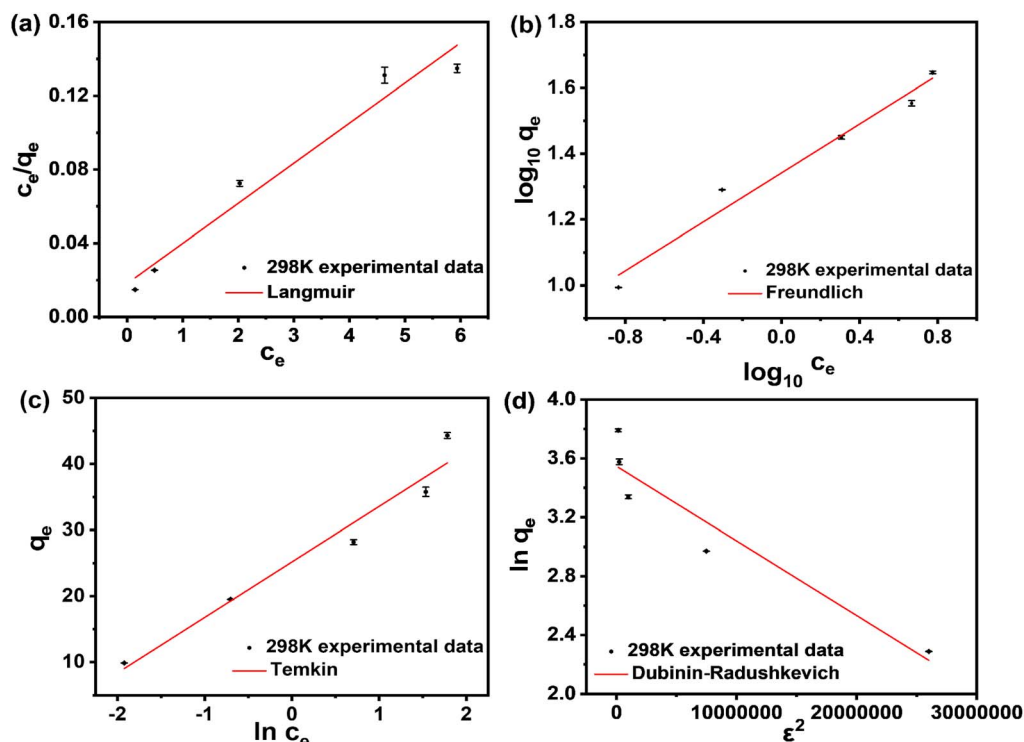
**Fig. 8** Fitting diagram of RhB adsorption isotherm models, (a) Langmuir model, (b) Freundlich model, (c) Temkin model and (d) D–R model.
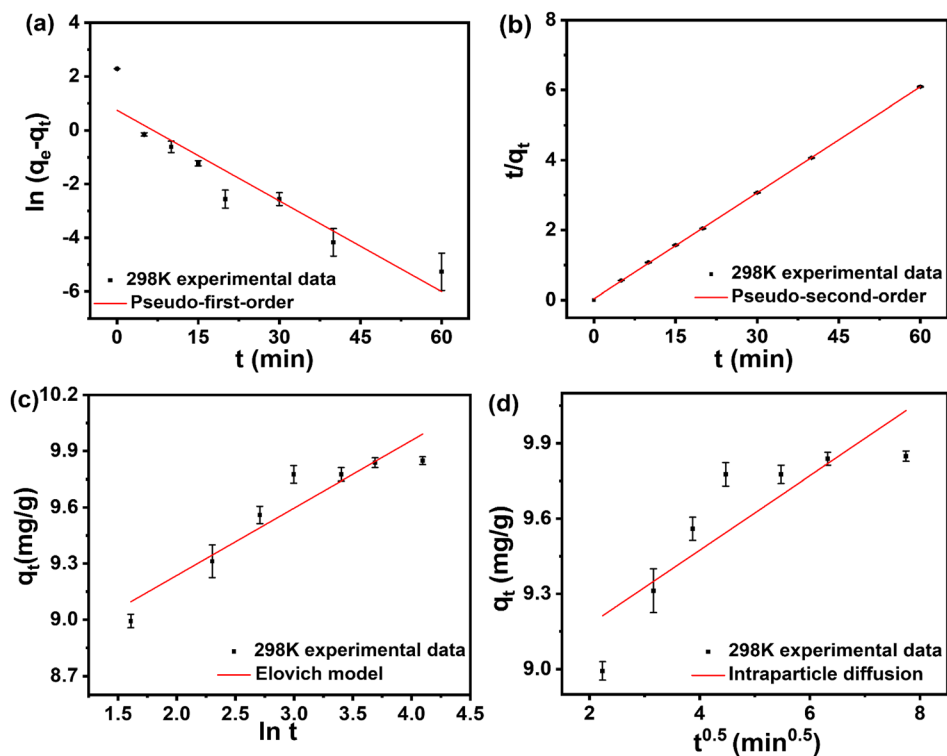


**Fig. 9** RhB adsorption kinetics model fitting diagram, (a) pseudo-first-order model, (b) pseudo-second-order model, (c) Elovich model and (d) intraparticle diffusion model.

first order rate constant. $k_2$ (g mg$^{-1}$ min$^{-1}$) is the pseudo-second order rate constant The values of $q_e$, $k_2$, and the correlation coefficients are summarized in Table 3. The pseudo-first-order and pseudo-second-order kinetic models are presented in Fig. 9(a) and (b). The $R^2$ values of the pseudo-first-order kinetic model and the pseudo-second-order kinetic model are 0.8699 and 0.9999 respectively. The high regression correlation coefficient for the pseudo-second-order model indicates that the adsorption of RhB dye molecules on the surface follows pseudo-second-order kinetics. Consequently, chemisorption serves as the primary rate-determining step. Specifically, the adsorption process involves chemical reactions occurring between the adsorbent and the adsorbate.[41] In the Elovich model, the parameter $\alpha$ (mg g$^{-1}$ min$^{-1}$) represents the initial adsorption rate, while $\beta$ (g mg$^{-1}$) denotes the desorption constant, which is associated with surface coverage and the activation energy of chemisorption. Fig. 9(d) illustrates the multi-step diffusion of RhB from the liquid phase to the solid surface and within the particle. Initially, diffusion occurs through the liquid film surrounding the adsorbent, indicating a momentary adsorption process. This is followed by diffusion into larger pores and finally into some internal pores. The curve does not pass through the origin, suggesting that this experiment involves both intra-particle diffusion and surface film diffusion processes, but these are not the sole rate-controlling steps.[42]

These comprehensive kinetic analyses collectively demonstrate that although multiple processes contribute to the adsorption mechanism, the pseudo-second-order model provides the most accurate description of the observed adsorption behavior, thereby highlighting the predominance of chemisorption in this system (Table 3).

### 3.7. Adsorption thermodynamics study

Thermodynamics links the adsorption isotherm to the equilibrium state, elucidating the spontaneity of the adsorption process. To explore the thermodynamic behavior of RhB adsorption onto HA0.5, a detailed thermodynamic analysis was performed for RhB at an initial concentration of 20 mg L$^{-1}$ across a temperature range of 25 to 45 °C. Gibbs free energy ($\Delta G^0$) is a critical indicator of the spontaneity of the adsorption process. The enthalpy change ($\Delta H^0$) reveals whether the reaction is endothermic or exothermic, while the entropy change ($\Delta S^0$) offers insight into the degree of disorder within the system. These thermodynamic parameters—Gibbs free energy ($\Delta G^0$), enthalpy change ($\Delta H^0$), and entropy change ($\Delta S^0$) can be quantitatively determined using the following equations.

It is evident that an increase in temperature from 298.15 to 318.15 K leads to a more negative $\Delta G^0$ for RhB adsorption,

indicating that higher temperatures improve the thermodynamic favorability of the adsorption process and enhance the affinity of HA0.5 for RhB. All $\Delta G^0$ values are negative, confirming that the adsorption process is thermodynamically favorable and spontaneous at all tested temperatures, with increased spontaneity as temperature rises (Table 4). Typically, $\Delta G^0$ values ranging from $-20$ to $0$ kJ mol$^{-1}$ suggest physical adsorption.[43] The positive enthalpy change ($\Delta H^0$) indicates that the adsorption process is endothermic. The positive value of $\Delta S^0$ reflects an increase in randomness at the solid–liquid interface due to RhB occupying active sites on the HA0.5 surface. This increase in randomness can be attributed to the greater translational entropy gained by displaced water molecules compared to the entropy loss associated with dye uptake.[44]

$$\Delta G^0 = -RT \ln K_c \qquad (4)$$

$$\mathrm{Ln}\, K_c = \Delta S^0/R - \Delta H^0/RT \qquad (5)$$

$$K_c = q_e/C_e \qquad (6)$$

### 3.8. Adsorption mechanism

The sulfate groups of SDS interact with the positively charged Ca$^{2+}$ ions in aqueous solution to form zwitterions. In the Ca$^{2+}$ rich domain, contact with PO$_4^{3-}$ ions in the aqueous environment promotes the formation of HAP particles. The electrostatic affinity between SDS and Ca$^{2+}$ ions facilitates the production of highly ordered HAP crystals.[45] Through the interaction between positive and negative charges in the reaction solution, the ($\equiv$P–O–) and ($\equiv$P–O–H) active sites on the HAP surface are significantly increased, leading to electrostatic interactions with the ($\equiv$N$^+$) groups of RhB. Simultaneously, the characteristic peak intensity of the (PO$_4^{3-}$) group decreases compared to its pre-
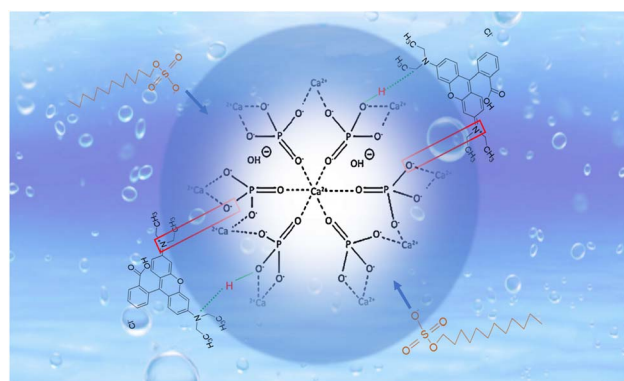


Fig. 10   Possible interaction between RhB and HA0.5.

**Table 4** Thermodynamic parameters for the RhB adsorption

| RhB (mg L$^{-1}$) | $\Delta G^0$ (kJ mol$^{-1}$) | | | | | $\Delta H^0$ (kJ mol$^{-1}$) | $\Delta S^0$ (J mol$^{-1}$ K$^{-1}$) |
|---|---|---|---|---|---|---|---|
| | 298.15 K | 303.15 K | 308.15 K | 313.15 K | 318.15 K | | |
| 20 mg L$^{-1}$ | $-9.9$ | $-11.9$ | $-12.4$ | $-13.2$ | $-14.6$ | 53.2 | 212.9 |

adsorption state. In the thermodynamic study, this experiment primarily involves physical adsorption, forming hydrogen bond interactions between the adsorbent's ($\equiv$P–OH) groups and the ($=$N) groups in RhB.[46] Additionally, there may be Lewis acid–base interactions involving $Ca^{2+}$ ions (Fig. 10).

## 4. Conclusion

In summary, SDS-HAP was synthesized *via* the sol–gel method to develop an adsorbent with superior biocompatibility, optimized microstructure, and high-efficiency dye adsorption capabilities. The incorporation of SDS significantly enhanced the dye adsorption capacity of pure HAP. Specifically, the mesoporous HA0.5 sample exhibited a specific surface area of 136.8 $m^2\ g^{-1}$ and an equilibrium adsorption capacity of 44.1 $mg\ g^{-1}$ for RhB. Experimental data showed excellent agreement with the Freundlich isotherm model, indicating multilayer adsorption behavior. The pseudo-second-order kinetic model accurately described the adsorption kinetics. Thermodynamic studies revealed that the adsorption process was spontaneous, endothermic, and predominantly physical in nature. Notably, unlike many other adsorbents, this material's performance was minimally affected by pH variations, a distinctive feature of HAP. It has the potential to remove various cationic dyes and is expected to become a green, efficient, and economical novel adsorbent, facilitating broader applications in environmental protection.

## Data availability

No data was used for the research described in the article.

## Author contributions

Ya-Ni Zhang: writing – original draft, visualization, methodology, formal analysis, and data curation; Qiu-Yan Yang and Peng Wang: investigation, methodology, writing – review & editing; Jia-Hui Li and Shu-Yao Zhang: supervision and project administration; En-Peng Deng and Xue-Min Wang: supervision, conceptualization; Jipeng Meng and Yu-Xin Miao: funding acquisition, writing – review & editing.

## Conflicts of interest

The authors declare no conflict of interest.

## Acknowledgements

## Notes and references

1 H. Zhang, P. Wang, Y. Zhang, *et al.*, *RSC Adv.*, 2020, **10**(67), 41251–41263.
2 Y. Liang, G. Huang, Q. Zhang, Y. Yang, J. Zhou and J. Cai, *J. Mol. Liq.*, 2021, **330**, 115580.
3 S. M. Hosseini, S. Vakili and A. Asadi, *RSC Adv.*, 2017, **7**(47), 29661–29669.
4 Z. G. Ren, F. Chen, B. Wang, *et al.*, *Environ. Eng. Res.*, 2020, **25**(4), 536–544.
5 Y. Liu and J. Yang, *Gels*, 2022, **8**(10), 675.
6 Y. Zhao, L. Zhu, W. Li, J. Liu, X. Liu and K. Huang, *J. Mol. Liq.*, 2019, **293**, 111516.
7 Y. W. Lin, S. Y. Peng and K. L. Lin, *J. Solid State Chem.*, 2024, **339**, 124914.
8 J. Mishra, D. S. Pattanayak, A. A. Das, *et al.*, *J. Mol. Liq.*, 2019, **287**, 110821.
9 M. Chahkandi, *Mater. Chem. Phys.*, 2017, **202**, 340–351.
10 J. Zheng, X. Wang, H. Qin, *et al.*, *Anal. Chem.*, 2024, **96**(45), 18011–18019.
11 F. Darvishalipour, H. Ghafouri Taleghani, M. Ghorbani and H. Salimi Kenari, *Int. J. Eng.*, 2019, **32**(2), 193–200.
12 X. Wang, J. Zheng, H. Qin, *et al.*, *Microchem. J.*, 2025, **209**, 112762.
13 F. Loosli and S. Stoll, *Environ. Sci.: Nano*, 2017, **4**, 203–211.
14 H. I. Elsaeedy, *Mater. Sci. Semicond. Process.*, 2019, **93**, 360–365.
15 A. U. Rajapaksha, S. S. Chen, D. C. Tsang, M. Zhang, M. Vithanage, S. Mandal, *et al.*, *Chemosphere*, 2016, **148**, 276–291.
16 G. Wang, J. Qi, S. Wang, *et al.*, *J. Dispersion Sci. Technol.*, 2017, **38**(5), 632–641.
17 M. Lakrat, H. Jodati, E. M. Mejdoubi and Z. Evis, *Powder Technol.*, 2023, **413**, 118026.
18 M. Kalpana and R. Nagalakshmi, *J. Indian Chem. Soc.*, 2023, **100**(4), 100947.
19 M. D. Prekajski, B. M. Jokić, A. Kalijadis, J. Maletaškić, N. Stanković, J. M. Luković, *et al.*, *Process. Appl. Ceram.*, 2016, **10**(3), 169–174.
20 D. Chlala, J.-M. Giraudon, N. Nuns, C. Lancelot, R.-N. Vannier, M. Labaki, *et al.*, *Appl. Catal., B*, 2016, **184**, 87–95.
21 Y. Xu, J. Wang, Z. Wang, Y. Zhao and W. Guo, *Eur. Polym. J.*, 2023, **187**, 111913.
22 W. Que, L. Jiang, C. Wang, Y. Liu, Z. Zeng, X. Wang, Q. Ning, S. Liu, P. Zhang and S. Liu, *J. Environ. Sci.*, 2018, **70**, 166–174.
23 A. Rodes, E. Pastor and T. Iwasita, *J. Electroanal. Chem.*, 1994, **376**(1–2), 109–118.
24 H. Zeghioud and S. Mouhamadou, *Water, Air, Soil Pollut.*, 2023, **234**(4), 233.
25 J. C. Y. Ng, W. H. Cheung and G. McKay, *J. Colloid Interface Sci.*, 2002, **255**(1), 64–74.
26 S. Chen, C. Qin, T. Wang, *et al.*, *J. Mol. Liq.*, 2019, **285**, 62–74.
27 T. A. Khan, S. Sharma and I. Ali, *J. Toxicol. Environ. Health Sci.*, 2011, **3**(10), 286–297.
28 M. E. Argun, S. Dursun, M. Karatas and M. Gürü, *Bioresour. Technol.*, 2008, **99**, 8691–8698.

29 D. Robati, M. Rajabi, O. Moradi, *et al.*, *J. Mol. Liq.*, 2016, **214**, 259–263.

30 Y. Bentahar, K. Draoui, C. Hurel, *et al.*, *J. Afr. Earth Sci.*, 2019, **154**, 80–88.

31 S. Chatterjee, A. Gupta, T. Mohanta, R. Mitra, D. Samanta, A. B. Mandal, M. Majumder, R. Rawat and N. R. Singha, *ACS Omega*, 2018, **3**(9), 11486–11496.

32 N. Abidin, N. S. Sambudi and N. A. Kamal, *ASEAN J. Chem. Eng.*, 2020, **20**, 140–153.

33 Y. Li, Y. Zhang, Y. Zhang, G. Wang, S. Li, R. Han and W. Wei, *J. Mol. Liq.*, 2018, **263**, 53–63.

34 T. A. Khan, S. Sharma and I. Ali, *J. Toxicol. Environ. Health Sci.*, 2011, **3**(10), 286–297.

35 H. B. Senturk, D. Ozdes, A. Gundogdu, C. Duran and M. Soylak, *J. Hazard. Mater.*, 2009, **172**(1), 353–362.

36 O. León, A. Muñoz-Bonilla, D. Soto, *et al.*, *Carbohydr. Polym.*, 2018, **194**, 375–383.

37 W. Xiao, Z. N. Garba, S. Sun, *et al.*, *J. Cleaner Prod.*, 2020, **253**, 119989.

38 L. Zhao, Q. Zhang, X. Li and J. Chen, *J. Hazard. Mater.*, 2020, **387**, 121808.

39 A. Masoumi and M. Ghaemy, *Carbohydr. Polym.*, 2014, **108**, 206–215.

40 I. Anastopoulos and G. Z. Kyzas, *J. Mol. Liq.*, 2014, **200**, 381–389.

41 J. H. Chen, Q. L. Liu, S. R. Hu, J. C. Ni and Y. S. He, *Chem. Eng. J.*, 2011, **173**, 511–519.

42 Y. Park, G. A. Ayoko, E. Horváth, R. Kurdi, J. Kristof and R. L. Frost, *J. Colloid Interface Sci.*, 2013, **393**, 319–334.

43 Y. Guesmi, H. Agougui, R. Lafi, M. Jablid and A. Hafiane, *J. Mol. Liq.*, 2018, **249**, 912–920.

44 A. A. Inyinbor, F. A. Adekola and G. A. Olatunji, *Water Resour. Ind.*, 2016, **15**, 14–27.

45 P. S. Prasad, B. C. G. Marupalli, S. Das, *et al.*, *J. Mater. Sci.*, 2023, **58**(14), 6076–6105.

46 P. Sharma and M. R. Das, *J. Chem. Eng. Data*, 2013, **58**, 151–158.